Journal of Hazardous Materials 296 (2015) 221–229

Contents lists available at ScienceDirect

Journal of Hazardous Materials

journal homepage: www.elsevier.com/locate/jhazmat

Fe-doped cryptomelane synthesized by refluxing at atmosphere: Structure, properties and photocatalytic degradation of phenol

Hui Yin[a], Xiaoxue Dai[a], Mengqiang Zhu[b], Feihu Li[c], Xionghan Feng[a,*], Fan Liu[a,*]

[a] Key Laboratory of Arable Land Conservation (Middle and Lower Reaches of Yangtze River), Ministry of Agriculture, College of Resources and Environment, Huazhong Agricultural University, Wuhan 430070, China
[b] Department of Ecosystem Science and Management, University of Wyoming, Laramie, WY 82071, USA
[c] School of Environmental Science and Engineering, Nanjing University of Information Science & Technology, Nanjing 210044, China

HIGHLIGHTS

- Fe-doped cryptomelanes were synthesized by refluxing at ambient pressure.
- Fe(III) exists both in the cryptomelane framework and in tunnel cavity.
- The UV–vis light absorption properties of doped cryptomelanes are greatly improved.
- Fe-doped cryptomelanes have enhanced ability in complete degradation of phenol.

GRAPHICAL ABSTRACT

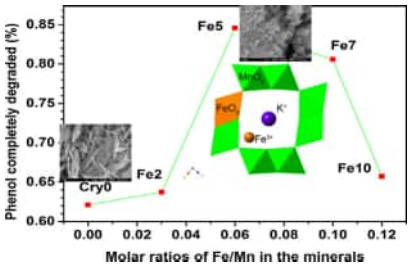

ARTICLE INFO

Article history:
Received 17 March 2015
Received in revised form 17 April 2015
Accepted 20 April 2015
Available online 23 April 2015

Keywords:
Cryptomelane
Fe doping
Powder X-ray diffraction
XAFS
Photocatalytic degradation

ABSTRACT

Fe-doped cryptomelanes were synthesized by refluxing at ambient pressure, followed by characterization with multiple techniques and test in photocatalytic degradation of phenol. The introduction of Fe(III) into the structure of cryptomelane results in a decrease in particle size and the contents of Mn and K^+, and an increase in the Mn average oxidation state (AOS), specific surface area and UV–vis light absorption ability. Mn and Fe K-edge extended X-ray absorption fine structure spectroscopy analysis indicates that some Fe(III) is incorporated into the framework of cryptomelane by replacing Mn(III) while the remaining Fe^{3+} is adsorbed in the tunnel cavity. These Fe-doped cryptomelanes have significantly improved the photocatalytic degradation rate of phenol, with the sample of ~3.04 wt.% Fe doping being the most reactive and achieving a degradation rate of 36% higher than that of the un-doped one. The enhanced reactivity can be ascribed to the increase in the coherent scattering domain size of the crystals, Mn AOS and light absorption, as well as the presence of sufficient K^+ in the tunnel. The results imply that metal doping is an effective way to improve the performance of cryptomelane in pollutants removal and has the potential for modification of Mn oxide materials.

1. Introduction

The cryptomelane-type octahedral molecular sieve (OMS-2) is a type of manganese oxide with edge- and corner-shared MnO_6 octahedra forming a 2 × 2 tunnel structure, with cations, such as K^+ and H^+ inside the tunnel for balancing the charge [1]. Due to the unique structural characteristics, such as large specific surface area (SSA), easy release of lattice oxygen and mixed valence of Mn, cryptomelane materials are widely used as adsorbents [2,3], oxidants [3,4], sensors [5] and catalysts [6–15].

Among all types of Mn oxides, cryptomelane shows the highest reactivity toward photocatalytic degradation of phenol in aqueous solution [10], which is a common organic pollutant in the environment with high toxicity, structural stability, and resistance to

* Corresponding authors. Tel.: +86 27 87280271; fax: +86 27 87280271.
E-mail address: liufan@mail.hzau.edu.cn (F. Liu).

http://dx.doi.org/10.1016/j.jhazmat.2015.04.055
0304-3894/

biodegradation [16]. The catalytic reactivity of cryptomelane with respect to this kind of pollutant is mainly affected by Mn AOS and lattice oxygen mobility [1], and it can also be influenced by light absorption [10,17], tunnel K^+ concentration [11], micromorphology [18], acidity, basicity and hydrophobicity [19].

Incorporation of cations into the structure of cryptomelane can alter its structure and physicochemical properties, and the dopants are usually located in the framework or tunnel cavity. On one hand, many high valence metal cations can be hydrothermally doped into the framework. Doping cryptomelanes with various types of cations can increase SSA and pore volume [20,21], modify Mn AOS [5,22,23] and thermal stability [20,22–24], increase structural defects, e.g., vacancies [5,24], and also enhance the reactivities of cryptomelane towards the catalytic oxidation of various organic pollutants [6,8,9,21]. On the other hand, the tunnel cavity of OMS-2 can accommodate some cations, such as K^+, Li^+, Na^+, Rb^+, Cs^+ and NH_4^+, which can also tailor the chemical and physical properties of the materials. Doping Li^+, Na^+, Rb^+, Cs^+ and NH_4^+ into the tunnels of cryptomelanes affect their crystallinity, SSA, thermal stability, and their catalytic activities for organic pollutants degradation [25,26]. Tunnel K^+ favors the stabilization of the α-MnO_2 structure [27], and can lead to a considerable improvement of the lattice oxygen activity and thus enhancing the catalytic activity for benzene oxidation [11].

In these previous studies, cryptomelanes were synthesized under hydrothermal conditions, which is rather problematic in terms of energy consumption and safety. In contrast, it is more favorable to synthesize cryptomelane by refluxing at low temperature under ambient pressure [28–32]. However, this may arouse questions, such as whether these metal cations can be incorporated into the cryptomelane framework or adsorbed in the tunnel cavity and how the structure and properties of the as-prepared cryptomelane would be affected. Here Fe-doped cryptomelanes were synthesized via refluxing at ambient pressure, and their structure and physicochemical properties were characterized by powder XRD, wet chemical analysis, field emission scanning electron microscopy (FE-SEM), N_2 adsorption, X-ray photoelectron spectroscopy (XPS), UV–vis diffuse reflectance spectroscopy (UV–vis DRS), and Fe and Mn K-edge extended X-ray absorption fine structure spectroscopy (EXAFS) analysis. The photocatalytic reactivity of these doped materials was also tested by degradation of phenol in aqueous solution. The overall results from this study have implications for modification of Mn oxide materials in contamination remediation and pollution control.

2. Materials and methods

2.1. Sample preparation and characterization

Fe-doped cryptomelanes were synthesized through reflux process under ambient pressure by adding $KMnO_4$ solution to mixtures of $Fe_2(SO_4)_3$, $MnSO_4$ and acetic acid at different molar ratios (Fe/Mn = 0, 0.02, 0.05, 0.07 and 0.10) as described in [3,33]. Typically 80 mL of 0.4375 mol/L $KMnO_4$ solution was heated to 60 °C and poured into 100 mL mixtures of 0.5 mol/L $Fe_2(SO_4)_3$ + $MnSO_4$ solutions (the molar ratio of Co/Mn is 0, 0.02, 0.05, 0.07 or 0.10) and 2 mol/L acetic acid which was also preheated at 60 °C. The mixtures were then heated and kept boiling under stirring for 20 min. A suitable amount of 2 mol/L acetic acid was added to make up the volatilized CH_3COOH during the reaction. All samples were washed with deionized water thoroughly, and then dried in oven at 60 °C for several days. After ground in an agate mortar to particle sizes below 100 mesh (154 μm), the products were stored in closed polyethylene plastic tubes at room temperature. Based on the initial molar ratios of Fe/Mn, the products were named as Cry0, Fe2, Fe5, Fe7 and Fe10, respectively.

Powder X-ray diffraction analysis of the samples was carried out on a Bruker D8 Advance diffractometer (λ = 0.15418 nm). The diffractometer was operated at a tube voltage of 40 kV and a current of 40 mA with 1.2 s counting time per 0.02° 2θ step. The Mn AOS was determined by the oxalate reduction-permanganate back-titration method [34]. Micromorphologies of the samples were probed by field emission scanning electron microscopy (Jeol JSM-6700F microscope) after being coated with a gold evaporated film. The SSAs and pore size distributions of the samples were obtained by analyzing the N_2 adsorption/desorption data using an Autosorb-1 standard physical adsorption analyzer after degassing 0.1–0.2 g samples at 110 °C for 3 h under vacuum. Chemical composition and XPS analysis were carried out as described in [35,36]. The UV–vis diffuse reflectance spectrum (UV–vis RDS) was measured by a Shimadzu 3600 spectrophotometer [10,37].

2.2. XAFS spectroscopy

The XAFS spectra of Fe-doped cryptomelanes were measured at room temperature at beamline 4-1 at the Stanford Synchrotron Radiation Lightsource (SSRL) [38]. Fe K-edge XAFS spectra were obtained in fluorescence mode over the range of 6912–7864 eV. The monochromator energy was calibrated to the first derivative of Fe metal foil (7112 eV) before every sample run. Mn K-edge XAFS data were collected in transmission mode over the energy range of 6339–7092 eV, which was somewhat short because of the interference of Fe absorption. The EXAFS spectrum of a Mn metal foil was collected (E_0 = 6539 eV) simultaneously with a reference ion chamber to calibrate the monochromator energy position.

EXAFS spectra were processed using the program Ifeffit/Athena [39]. Parameters used for background removal of Fe K-edge spectra were: E_0 = 7126 eV, R_{bkg} = 1.0 Å and k-weight = 2. Then the XAFS spectra were converted into the k^3-weighted function and FTs were calculated over a k range of 2.0–11.0 $Å^{-1}$ and a R range of 1–6 Å. Mn K-edge spectra were background-subtracted using the following parameters: E_0 = 6557 eV, Rbkg = 1.0 Å and k-weight = 2. The XAFS spectra were converted into the k^3-weighted function and FTs were calculated over a k range of 2.4–11.1 $Å^{-1}$ and a R range of 1–6 Å. Structural parameters (R, CN, and Debye–Waller factor, σ^2) were obtained by fitting the experimental k^3-weighted EXAFS spectra to the standard EXAFS equation [40] implanted in SIXPack [41], using several single-scattering paths over a R range of 1–4 Å for both Fe and Mn. Phase and amplitude functions for single-scattering paths were calculated based on cryptomelane structure using FEFF7 [42].

2.3. Photocatalytic degradation of phenol

The photocatalytic degradation experiments of phenol by these materials were carried out as described in [10,37]. Briefly, in a 50-mL quartz tube, 5 mL of 500 mg L^{-1} phenol solution (pH 6.00 ± 0.05) was mixed with 20 mL of 1.25 g L^{-1} mineral suspension (prepared by dispersion of 0.025 g Fe-doped cryptomelane into 20 mL of deionized water, and the pH of the suspension was then adjusted to 6.00 ± 0.05). Then all the quartz tubes were placed on a SGY-1 rotary photochemical reactor and ventilated with air at a steady rate of 3.3 L min^{-1}. The photocatalytic reaction was conducted with the radiation of a 300 W high-pressure mercury lamp. After reaction for 12 h, the suspensions were centrifuged (10,000 × g, 5 min), and the supernatant was filtered through a 0.22-μm membrane for total organic carbon (TOC) analyses. TOC removal rate was used to evaluate the photocatalytic degradation of phenol by these materials. Duplicates were conducted and the average was used. The TOC removal rate was calculated by: $C_{Toc} = (C_0 - C_t)/C_0 \times 100\%$, in which C_0 (mg L^{-1}) and C_t (mg L^{-1}) are the initial and final TOC concentrations, respectively.

Table 1
Rietveld structural refinement results of unit-cell parameters, crystal sizes and cell volumes of Fe-doped cryptomelanes.

Sample	a (Å)	b (Å)	c (Å)	β (°)	CrySize[a] (nm)	Cell volume (Å^3)	R_{wp}[b] (%)
Cry0	9.9487(46)	2.8529(32)	9.6748(50)	91.511(25)	12.24(21)	274.50(36)	5.39
Fe2	9.9098(33)	2.8516(6)	9.6713(35)	91.338(17)	17.37(30)	273.22(14)	6.24
Fe5	9.8665(22)	2.8522(4)	9.6711(30)	91.050(16)	19.08(27)	272.11(11)	4.84
Fe7	9.8607(27)	2.8532(4)	9.6740(36)	91.011(18)	16.02(19)	272.13(13)	3.69
Fe10	9.8772(45)	2.8543(7)	9.6714(58)	91.112(29)	12.92(17)	272.61(22)	3.27

[a] The average coherent scattering domain (CSD) sizes modeled using Lorentzian function.

[b] R_{wp} indicates the quality of fitting and is expressed by $R_{wp} = \sqrt{\frac{\sum w_i(Y_{o,i}-Y_{c,i})^2}{\sum w_i Y_{o,i}^2}}$.

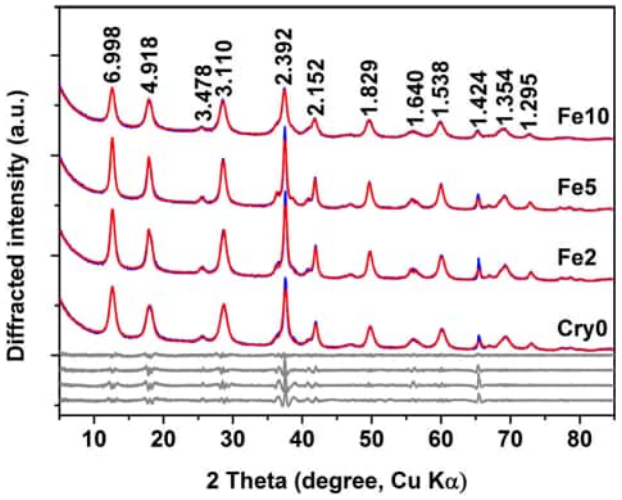

Fig. 1. Rietveld structural refinement of Fe-doped cryptomelanes (unit for d-spacing is Å. Blue lines are experimental data, red lines are calculated patterns and gray lines are difference patterns). (For interpretation of the references to color in this figure legend, the reader is referred to the web version of this article.)

3. Results and analysis

3.1. Powder XRD

Fig. 1 presents the powder XRD patterns of the Fe-doped samples. Each of the patterns matches quite well with that of the standard cryptomelane (JCPDS 74-1451). There are no additional peaks in the XRD patterns, indicating that no impurity is present and that Fe has not modified the structure of cryptomelane. However, with an increase in the dopant content, some changes can be observed in the diffraction intensities and the full widths at half maximum (FWHM). When the molar ratios of Fe/Mn $\leq$ 0.05, there is an increase in peak intensity and a decrease in FWHM; with a further increase in the Fe content, there appears a decrease in the diffraction intensity and an increase in FWHM. This suggests that Fe doping can lead to an increase first and then a decrease in the coherent scattering domain (CSD) size of doped cryptomelane crystals.

Based on the standard cryptomelane structure with monoclinic symmetry (I2/m), Rietveld structure refinement of these Fe-doped cryptomelanes was conducted using software TOPAS, and the results are shown in Fig. 1 and Table 1. With increasing dopant content, the lattice parameters a, β and cell volumes of doped cryptomelanes slightly decrease while b and c remain unchanged. The calculated CSD size for Cry0 is ~12 nm, then is increased to ~19 nm for Fe5, and then is decreased to ~13 nm for Fe10 (Table 1).

3.2. Elemental analysis and Mn AOS

The results of elemental analysis and Mn AOSs of these Fe-doped cryptomelanes are detailed in Table 2. The final molar ratios of Fe/Mn generally agree well with the initial ratios. With increasing Fe contents, the Mn contents in these doped cryptomelanes gradually decrease. From Cry0 to Fe5, the molar ratios of K/Mn are almost the same (0.032–0.033), but for Fe7 and Fe10, the K/Mn molar ratios decrease to 0.024–0.025. Just as the K^+ content in the interlayer regions of hexagonal birnessites can be used as an index to simply and qualitatively judge the spatial distribution of transitional metals (TM) in the birnessite structure, so the variations in the tunnel K^+ content in the cryptomelane can reflect whether the dopants are incorporated into the framework or located in the tunnel cavity. For the hydrothermal cryptomelanes, the K^+ content increases with increasing Fe [22,23], and Fe is proved to have the same atomic coordination environments as framework Mn by anomalous XRD and Mössbauer spectra [23]. In the V(V)-doped cryptomelanes, the increase of vanadium content is well correlated with a reduction in Mn percentage but a relatively constant K^+ concentration. This indicates that V is isomorphously substituting for Mn in the framework [5]. For the Fe-doped cryptomelanes here, the decrease in K^+ content indicates that part of the dopants is adsorbed in the tunnels.

The Mn AOS of Cry is 3.83. Fe doping gradually increases the Mn AOSs. This suggests that Fe(III) is incorporated into the framework of cryptomelane by replacing Mn(III) and/or into the tunnel by replacing $Mn^{3+/2+}$.

3.3. Morphology, SSA and micropore size

The FE-SEM images of these samples are displayed in Fig. 2. As shown in Fig. 2a, Cry0 is composed of uniform needle crystals. With increasing Fe content, the needle crystals of Fe2 decrease in length but increase slightly in width (Fig. 2b), and then the

Table 2
Elemental analysis, Mn AOSs and SSAs of Fe-doped cryptomelanes.

Sample	Element content (%)			Fe/Mn molar ratio	Mn AOS	SSA (m^2/g)	Micropore size (nm)
	Mn	Fe	K				
Cry0	56.97	0	1.30	0	3.83	139	0.48
Fe2	56.03	1.62	1.30	0.03	3.84	134	0.46
Fe5	53.32	3.04	1.24	0.06	3.85	124	0.46
Fe7	51.06	5.12	0.86	0.10	3.87	163	0.48
Fe10	48.92	5.97	0.86	0.12	3.88	221	0.46

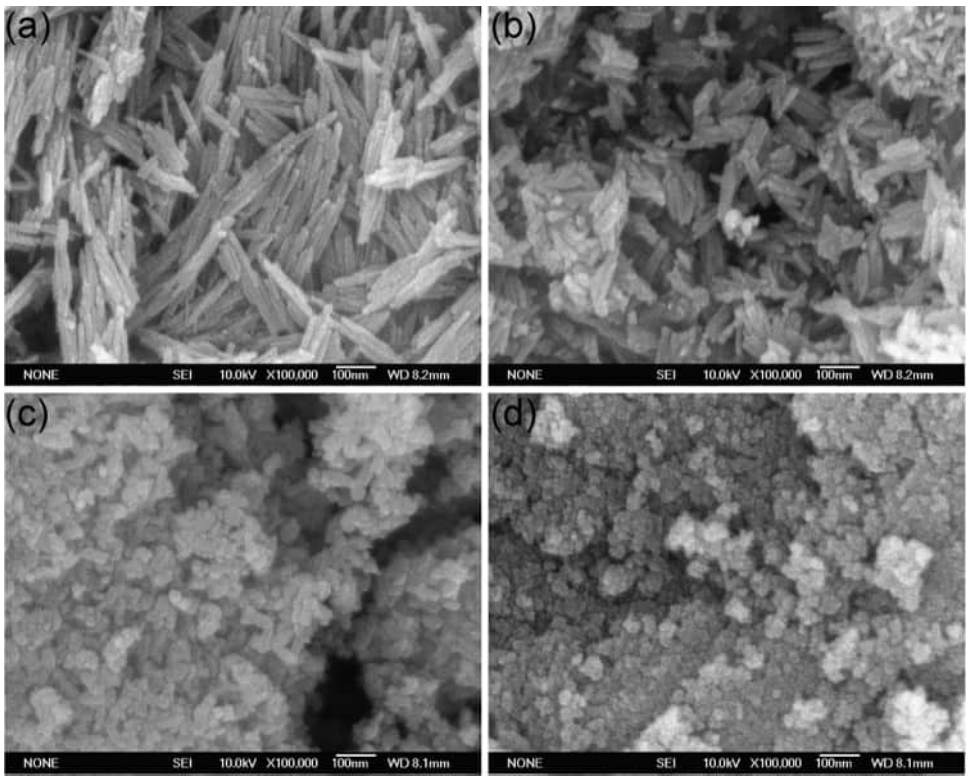

Fig. 2. FE-SEM images of Fe-doped cryptomelane samples. (a) Cry0, (b) Fe2, (c) Fe5 and (d) Fe10.

Fe-doped samples become granular particles with aggregation (Fig. 2c and d). It is observed that the particle sizes of these Fe-doped cryptomelanes are generally decreased. This spuriously contradicts with the results of qualitative analysis of powder XRD profiles and the Rietveld structure refinement. Actually the average crystal sizes obtained by XRD analysis reflect the CSD sizes of the crystals whereas the SEM observes the actual physical dimensions of the crystals. The two "sizes" are always different attributed to structure disorder in the crystal structure [43,44] and the shapes of the crystals.

The SSA of Cry0 is 139 $m^2\,g^{-1}$, and those of the doped samples generally increase with increasing Fe content. When the initial Fe/Mn is increased to 0.10, the SSA is increased to 221 $m^2\,g^{-1}$ (Table 2). The N_2 adsorption-desorption curves of these materials are listed in Fig. 3 and Fig. S1, and all of them are typical IV curves.

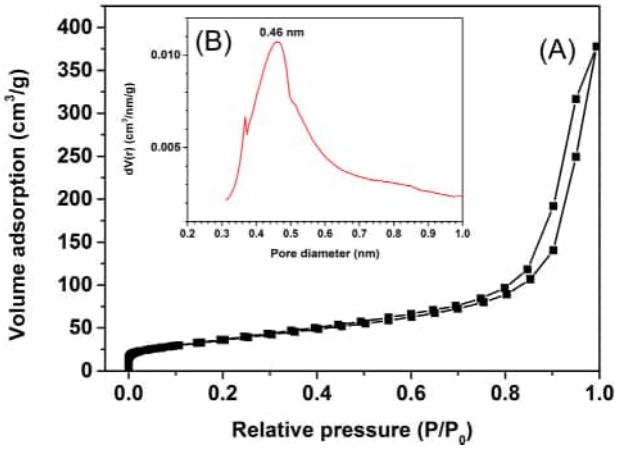

Fig. 3. (A) N_2 adsorption–desorption isothermal curves of Fe2 and (B) corresponding micropore size distribution calculated by the Horvath–Kawazoe (HK) method.

Micropore analysis is conducted based on the Horvath–Kawazoe (HK) using the adsorption branch [29]. The micropore diameters of the doped OMS-2 materials are 0.46–0.48 nm, matching quite well with the tunnel size of cryptomelane (0.46 nm × 0.46 nm).

3.4. Mn ($2p_{3/2}$) and Fe (2p) XPS Spectra

The Mn ($2p_{3/2}$) spectra of these Fe-doped cryptomelanes are shown in Fig. 4 and Fig. S2. By multiple peak fitting, the relative percentages of Mn^{2+}, Mn^{3+} and Mn^{4+} on the mineral surfaces can be quantified [45]. Multiplet parameters from [35] are used, and the fitting results are demonstrated in Fig. 4, Fig. S2, Table 3 and Table S1. It shows that the percentage of Mn^{4+} on the mineral surface increases while those of Mn^{3+} and Mn^{2+} decline with increasing Fe content. The Mn AOSs for Cry0, Fe2, Fe5, Fe7 and Fe10 are calculated to be 3.62, 3.64, 3.67, 3.67 and 3.71, respectively, which coincide well with those obtained by titration.

Fe (2p) narrow scans are presented in Fig. 4. Two peaks are well characterized for the doped samples, with the maxima of the peaks for Fe ($2p_{1/2}$) and Fe ($2p_{3/2}$) located at 724.6 and 711.1 eV, respectively. These values match quite well with those of FeOOH reported by Tan et al. (1990) [46], suggesting that Fe mainly exists in a valence of +3 in these materials.

Table 3
Near-surface composition of Mn obtained by fitting the Mn ($2p_{3/2}$) spectra of Fe-doped cryptomelanes

Sample	Mn^{2+} (At.%)	Mn^{3+} (At.%)	Mn^{4+} (At.%)
Cry0	12.78	12.04	75.18
Fe2	6.17	23.52	70.28
Fe5	6.78	18.64	74.50
Fe7	9.07	14.64	76.20
Fe10	9.21	10.05	80.75

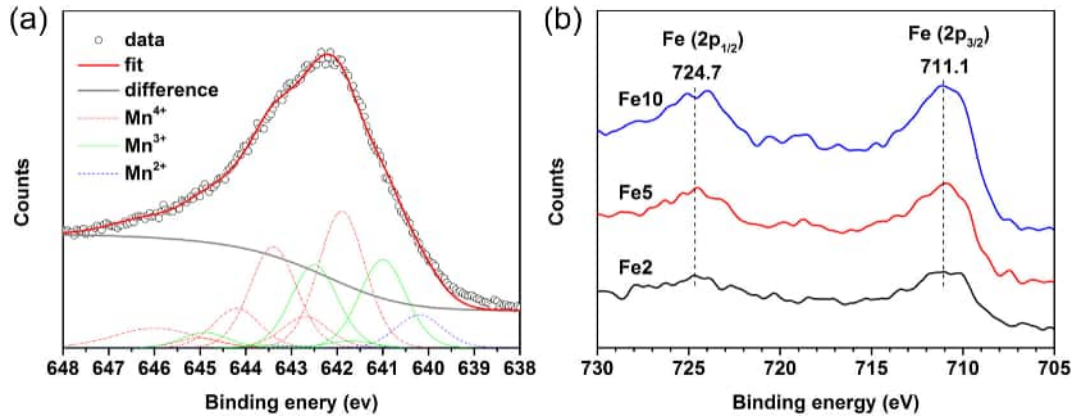

Fig. 4. (a) Mn ($2p_{3/2}$) spectrum of sample Fe2 with the best fit overlaid (The upper circles represent observed data and the thick, solid curve is the best fit to the data. The red dash-dot curves represent Mn(IV) multiplet peaks, green thin solid curves Mn(III) and blue dotted lines Mn(II)), and (b) Fe (2p) spectra of these Fe-doped cryptomelanes. (For interpretation of the references to color in this figure legend, the reader is referred to the web version of this article.)

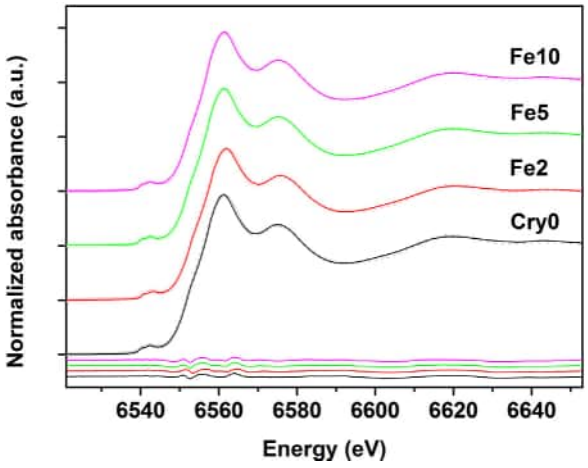

Fig. 5. Linear combination fit of the Mn K-edge XANES spectra of Fe-doped cryptomelanes using the Combo method [47] in the 6521–6653 eV interval (circles are experimental data, and solid lines are the best fits. The differences between the experimental data and the best fits are shown at the bottom).

3.5. EXAFS spectroscopy

3.5.1. Mn K-edge XAFS

Fig. 5 shows the Mn K-edge XANES spectra of Fe-doped cryptomelanes. The Combo method [47] was also used to determine the relative proportions of Mn^{2+}, Mn^{3+} and Mn^{4+} in these minerals. Fitting results are given in Fig. 5 and Table S2. The Mn K-edge XANES spectra of Cry0, Fe2, Fe5, Fe7 and Fe10 can be best reconstructed individually by 88.73% Mn^{4+} + 11.27% Mn^{3+}, 87.89% Mn^{4+} + 12.11% Mn^{3+}, 95.26% Mn^{4+} + 4.74% Mn^{3+}, 95.08% Mn^{4+} + 4.92% Mn^{3+} and 98.20% Mn^{4+} + 1.80% Mn^{3+}. This suggests that the doped cryptomelanes are composed predominantly of Mn^{4+} with a small amount of Mn^{3+} but no Mn^{2+}. With increasing Fe content, the percentage of Mn^{4+} increases, but that of Mn^{3+} decreases. This confirms that incorporated Fe(III) replaces low valence Mn in the framework and tunnel. Based on the fitting results, the Mn AOSs of these Fe-doped cryptomelanes are 3.89, 3.88, 3.95, 3.95 and 3.98, respectively, which agree well with the results obtained by the titration method. The Mn ($2p_{3/2}$) XPS analysis shows that there is some Mn^{2+} on the mineral surface, which might originate from the reduction of high valence Mn to Mn^{2+} induced by X-ray radiation [35,47].

Mn K-edge EXAFS spectra and FTs are presented in Fig. 6A and B. The k^3-weighted EXAFS spectra possess the basic oscillation features of cryptomelane [48]. In the FTs, the three prominent peaks located at $R+\Delta R$ ~1.5 Å, ~2.4 Å and ~3.0 Å are ascribed to Mn–O distances in [MnO_6] unit and edge- and corner-sharing Mn–Me (Me = Mn, Fe) pairs, respectively [7,23,49]. With increasing Fe content, the $R+\Delta R$ ~2.4 Å and ~3.0 Å peaks slightly shift right, indicating an increase in the distances of edge- and corner-sharing Mn–Me pairs.

Fitting results of Mn K-edge EXAFS spectra are presented in Fig. 6 A, B and Table S3. The Mn–O distance in [MnO_6] octahedra of these Co-doped cryptomelanes is 1.892 Å. The edge- and corner-sharing Mn–Me distances for Cry0 are 2.881 Å and 3.442 Å, consistent well with previous reports [7,23,49]. Upon Fe doping, the distance of edge-sharing Mn–Me (Mn–Me1) increases from 2.882 Å to 2.886 Å while that of corner-sharing Mn–Me (Mn–Me2) increases from 3.444 Å to 3.446 Å. This is mainly caused by the substitution of framework Mn(III) by Fe(III), with the crystal radius of the latter (0.785 Å) being larger than that of the former (0.72 Å) [50].

3.5.2. Fe K-edge EXAFS

Fe K-edge EXAFS spectra of these samples are presented in Fig. 6C and D. The frequencies of these spectra differ from those of Mn K-edge EXAFS spectra, indicating that the local atomic environments of Fe are quite different from those of Mn. Since there are two equivalent Mn sites in the cryptomelane framework and if Fe unselectively substitutes for either Mn site, the oscillations of Fe and Mn K-edge EXAFS spectra should be similar to those of Co and Mn in the manganese layers of the birnessite [7,36,51]. Therefore, it can be concluded that Fe does not occupy unselectively the two crystallographic Mn sites in the framework, and/or some dopants are located in the tunnel cavity.

In the FTs, three major peaks are located at $R+\Delta R$ ~1.5 Å, ~2.4 Å and ~3.0 Å, which are corresponding to Fe–O in [FeO_6] octahedron, edge-sharing Fe–Me pairs (Fe–Me1) and corner-sharing Fe–Me pairs (Fe–Me2). The existence of the $R+\Delta R$ ~2.4 Å peak confirms the incorporation of Fe into the framework, and the bond lengths of Fe–O, Fe–Me1 and Fe–Me2 increase with increasing Fe content.

The results of the fitting of these Fe K-edge EXAFS spectra are presented in Fig. 6C and D and Table 4, showing that, with the increase of the Fe content from Fe5 to Fe10 in these doped cryptomelanes, the Fe–O distance in [FeO_6] octahedron increases from 1.934 Å to 1.953 Å, the Fe–Me1 distance from 2.882 Å to 2.921 Å, and the Fe–Me2 distance from 3.388 Å to 3.410 Å. This phenomenon is also observed in the EXAFS analysis of hydrothermally synthesized Fe-doped cryptomelanes [23]. The Fe–O distances in these Fe-doped cryptomelanes are longer than the Mn–O distances but shorter than the Fe–O distances in Fe oxides [23,52]. The Fe–Me1 distance in Fe5 is very close to that of Mn–Me1, but those of Fe7

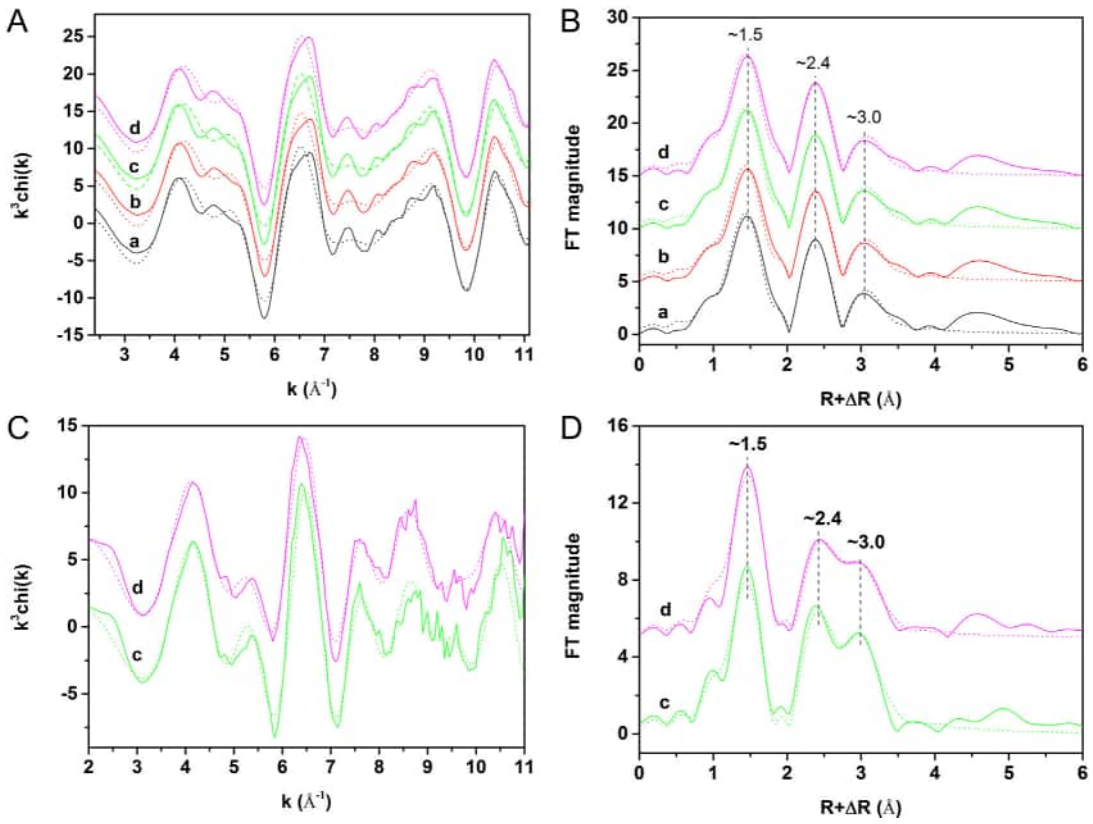

Fig. 6. Mn K-edge (A) and Fe K-edge (C) EXAFS spectra and the corresponding Fourier transformed spectra (FTs) (B and D) of Fe-doped cryptomelanes (the solid lines are experimental data and the dotted lines are best fit)
a: Cry0; b: Fe2; c: Fe5; d: Fe7 and e: Fe10.

and Fe10 are increased by ~0.04 Å. Due to the similar X-ray scattering factors of Fe and Mn atoms, the signals of Mn–O and Mn–Me1 are overlapped with those of Fe–O and Fe–Me1. Incorporation of more Fe(III) into the cryptomelane framework by replacing Mn(III) greatly contributes to the increase of the Fe–Me1 distance. However, the Fe–O and Fe–Me1 distances of Fe10 do not increase as much as those of Fe7, probably because part of the Fe^{3+} cations are located in the tunnels. Furthermore, in our Fe-doped cryptomelanes, Fe–Me2 bond lengths are shorter than those of Mn–Me2. This is contrary to the observation in the hydrothermally synthesized Fe-doped analogies, in which almost all Fe is incorporated into the framework [23]. This finding further confirms that the Fe in our doped cryptomelanes exists in both framework and tunnel cavity, which is already qualitatively indexed by the variations in tunnel K^+ contents. However, the Fe–Mn distance for the Fe^{3+} in cryptomelane tunnels cannot be distinguished from that of Fe–Me2 in this work. It is reported that, in Cd^{2+}-sorbed cryptomelanes, Cd^{2+} is located inside the tunnels and has 4.9 Mn atoms at 3.65 Å [2]. Based on the difference in crystal radii of Cd^{2+} (1.09 Å) and Fe^{3+} (0.785 Å) and our EXAFS fitting results, the distance between tunnel Fe^{3+} and nearest framework Mn is ~3.39–3.41 Å.

3.6. UV–vis DRS analysis

Among various Mn oxides, cryptomelane shows the strongest ability of light adsorption in the range of 250–800 nm [10]. The

Table 4
Structure parameters derived from Fe K-edge EXAFS fitting over 1–4 Å of Fe-doped cryptomelanes.

Atomic pairs	Fe5	Fe7	Fe10	
Fe–O	CN	6	6	6
	R (Å)	1.934(0.015)	1.953(0.012)	1.953(0.012)
	σ^2 (Å^2)	0.0082(0.0011)	0.0064(0.0009)	0.0075(0.0009)
Fe–Me[a]1	CN	2.4(1.6)	3.5(2.1)	2.8(1.5)
	R (Å)	2.882(0.024)	2.922(0.021)	2.921(0.020)
	σ^2 (Å^2)	0.0041(0.0042)	0.0087(0.0047)	0.0067(0.0040)
Fe–Me2	CN	4.6(2.6)	4.2(2.3)	2.9(1.7)
	R (Å)	3.388(0.021)	3.406(0.018)	3.410(0.017)
	σ^2 (Å^2)	0.0051(0.0038)	0.0063(0.0041)	0.0043(0.0041)
ΔE_0		−7.3(2.4)	−5.2(2.0)	−5.2(1.9)
(eV)		395.61	407.70	469.53
Chi sq				
R factor		0.0351	0.0312	0.0297

[a] Me = Mn, Fe for the X-ray scattering factors of Mn and Fe are similar, and it is difficult to differentiate them.

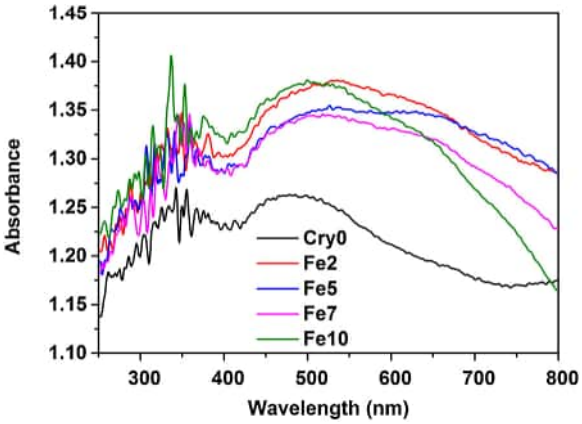

Fig. 7. UV–vis DRS spectra of Fe-doped cryptomelanes.

UV–vis DRS of these Fe-doped materials are drawn in Fig. 7. The absorption curves indicate a flat absorption, suggesting that these materials have perfect ability in light absorption and are ideal for photocatalysis. Further, in the whole Fe doping range, the curves of the doped cryptomelanes are higher than that of the un-doped one, indicating that Fe doping greatly enhances the light absorption.

Light absorption properties of these doped cryptomelanes may be affected by many factors. First, insertion of exotic cations into the framework of cryptomelanes will induce structural defects, such as vacancies [5,24]. These structural defects will promote the separation of photo-induced electrons and holes, thus hindering the recombination of these charge-carriers, and then increase the concentration of photo-induced electrons, and finally improve the reactivity in photocatalytic reactions [53]. Second, the light absorption is also affected by the CSD sizes of crystals of the catalyst due to remarkable differences of the optical properties of the bulk and the nanostructured MnO_2 materials. The absorption of the MnO_2 colloid at longer wavelengths strongly decreases as the CSD sizes of the MnO_2 particles decrease [54]. This is obvious for the Fe10 sample here, whose light absorption over 600–800 nm remarkably declines with the decrease of its CSD size. Finally, the light absorption may also be influenced by the variations in the valence of Mn ions, the contents of water and K^+ in the structure of cryptomelane and so on [55].

3.7. Photocatalytic degradation of phenol from wastewaters

The photocatalytic degradation experiments of phenol by these Fe-doped cryptomelanes were conducted in simulated wastewaters. According to previous reports [16,56–58], besides the final non-toxic products of CO_2 and H_2O, many intermediates are produced during photocatalytic degradation of phenol, which mainly include biphenols, quinones and/or low molecular weight organic acids, etc. These intermediates, however, are also environmental contaminants. Therefore, the TOC removal rate, the fraction of phenol that is totally degraded to CO_2 and H_2O, is the most practical index to evaluate the performance of the doped materials in detoxifying organic pollutants like phenol in the environment.

After 12 h reaction under UV–vis light irradiation (the high-pressure mercury lamp used in this experiment has relatively high irradiation at 366 nm, 436 nm, 546 nm and 578 nm), the TOC removal rates of Cry0, Fe2, Fe5, Fe7 and Fe10 are 62.12%, 63.72%, 84.57%, 80.57% and 65.72%, respectively, showing that, with increasing Fe content, the TOC removal rates first increase, followed by a decrease, with the highest TOC removal rate observed for Fe5. The results demonstrate that a certain amount of Fe doping can greatly improve the ability of cryptomelanes in removing phenol from wastewaters. The TOC removal rates of these Fe-doped cryptomelanes are higher than those of birnessite and todorokite [10], Ce-doped cryptomelanes [59], mixtures of manganite and hausmannite [60]. These Fe-doped cryptomelane materials hold great promise for the remediation of water systems polluted by organic compounds, such as phenol.

4. Discussion

Fe(III) is introduced into the structure of cryptomelane by refluxing at ambient pressure. These doped cryptomelanes have reduced the particle size and increased SSA. Upon doping, the contents of Mn and K^+ in the minerals are greatly decreased. This is quite different from the hydrothermally synthesized Fe-doped cryptomelanes [23], in which almost all Fe is doped into the framework and the molar ratio of K^+/Mn is greatly increased. So the decrease in the tunnel K^+ content means that part of the Fe^{3+} is adsorbed in the tunnel cavity of cryptomelane to more effectively neutralize the negative charge of the framework. Further titration, Mn ($2p_{3/2}$) XPS, and Mn K-edge XNAES analyses show that the Mn AOS of cryptomelane is increased after doping, suggesting that Fe may be incorporated into the framework by replacing Mn(III) and/or into the tunnel by ion-exchange with Mn^{3+}. This is further confirmed by quantitative analysis of Fe K-edge EXAFS spectra. In FTs, the existence of peak at R ~2.88–2.92 Å confirms the insertion of Fe into the framework, and the existence of peak at R ~3.39–3.41 Å indicates the location of some Fe^{3+} in the tunnel. The incorporation of part of Fe in the framework, the location of some Fe in the tunnel, and the decrease of the K^+ content may importantly contribute to the decrease in lattice parameters a, β and cell volume.

These Fe-doped cryptomelanes have enhanced the total removal of phenol from wastewaters, i.e., the TOC removal rate is increased by 36% when the initial molar ratio of Fe/Mn is 0.05. The photocatalytic reactivity of these Fe-doped cryptomelanes is affected by many factors. Firstly, owing to the mixed valence of Mn, high valence Mn in Fe-doped cryptomelanes can be directly reduced by obtaining electrons from organic pollutants, such as phenol. The higher the Mn AOS for cryptomelane, the more favorable will be the oxidation reaction. Fe doping greatly increases the Mn AOS, and thus promotes the direct oxidation of phenol. Secondly, the catalyst with large SSA is generally considered to have more active sites exposed, and thus facilitates reaction [61]. However, Fe10 has the largest SSA, but its TOC removal rate is quite low, indicating that SSA is not the controlling factor for the TOC removal rate. Thirdly, as discussed in Section 3.6, CSD sizes of the catalyst crystals also influence the light absorption properties. With increasing Fe content, the CSD sizes of these materials first increase and then decrease. When the molar ratio of Fe/Mn is increased to 0.10, the CSD size of Fe10 is greatly decreased, leading to a significant attenuation in its light absorption, which contributes to the low TOC removal rate. Fourthly, the chemical composition, especially K^+ content, has an important effect on the catalytic reactivity. It is recently reported that, increasing the K^+ concentration leads to a considerable enhancement of the lattice oxygen activity in OMS-2 nanorods, and thus a significant enhancement of the catalytic activity for benzene oxidation [11]. The final molar ratios of K/Mn are 0.032, 0.033, 0.033, 0.024 and 0.025 for Cry0, Fe2, Fe5, Fe7 and Fe10, respectively. In the structures of Fe7 and Fe10, part of Fe^{3+} is located in the tunnel and the tunnel K^+ content is decreased, leading to the decrease of their lattice oxygen activities and the catalytic activities. Finally, but not the least important, is the light absorption properties of these doped cryptomelanes, which are affected by the aforementioned factors, including Mn AOS, CSD size, K^+ content, and structural defects and so on. The light absorption of these doped cryptomelanes is significantly improved by Fe doping as compared to that of the un-doped one. Upon illumination, the photocatalytical reaction is initiated by the excitation of the occupied electrons on O (2p) of

the Mn oxides to the unoccupied orbits (mainly Mn (3d)) with the photo-induced active oxygen species accepting the electrons from phenol. When the catalysts with excellent light absorption properties are illuminated, more active oxygen species can be excited, and the catalysts show higher photocatalytic activities in degradation of phenol [53,62]. Therefore, introducing a certain amount of Fe into the structure of cryptomelane facilitates the total removal of phenol from wastewaters by increasing the crystal CSD size, Mn AOS and light absorption properties, and maintaining the K^+ content.

5. Conclusions

- Fe-doped cryptomelanes are synthesized with a series of Fe/Mn molar ratios by refluxing at ambient pressure.
- Fe doping has significant effects on the physicochemical properties of cryptomelane by decreasing the particle size and the contents of Mn and K^+, increasing Mn AOS and SSA, and slightly modifying the microstructure parameters, such as decreasing the lattice parameters a, β and cell volume.
- Upon Fe doping, the edge-sharing and corner-sharing Mn–Me distances in the cryptomelane structure are slightly increased, with part of Fe(III) incorporated into the framework by replacing the crystallographic Mn(III) sites, and the rest adsorbed in the tunnel cavity.
- The synergy of the great enhancement in UV–vis light absorption properties of these Fe-doped cryptomelanes, the increase in the CSD sizes and Mn AOS, and the maintenance of sufficient K^+ in the tunnel contributes to the significant improvement in the TOC removal rate during the photocatalytic degradation of phenol by the Fe5 sample. The cryptomelane doped with a certain amount of Fe has a great potential for application in treating water systems polluted by organic pollutants, such as phenol.

Acknowledgements

The authors gratefully thank the Natural Science Foundation of China (Grants 41271253 and 41401250), and Huazhong Agricultural University Doctoral Start-Up Fund (Grant 52902-0900206162) for financial support.

Appendix A. Supplementary data

Supplementary data associated with this article can be found, in the online version, at http://dx.doi.org/10.1016/j.jhazmat.2015.04.055.

References

[1] S.L. Suib, Porous manganese oxide octahedral molecular sieves and octahedral layered materials, Acc. Chem. Res. 41 (2008) 479–487.
[2] S.R. Randall, D.M. Sherman, K.V. Ragnarsdottir, An extended X-ray absorption fine structure spectroscopy investigation of cadmium sorption on cryptomelane (KMn8O16), Chem. Geol. 151 (1998) 95–106.
[3] X.H. Feng, L.M. Zhai, W.F. Tan, F. Liu, J.Z. He, Adsorption and redox reactions of heavy metals on synthesized Mn oxide minerals, Environ. Pollut. 147 (2007) 366–373.
[4] E. Deschamps, V.S.T. Ciminelli, W.H. Höll, Removal of As(III) and As(V) from water using a natural Fe and Mn enriched sample, Water Res. 39 (2005) 5212–5220.
[5] M. Polverejan, J.C. Villegas, S.L. Suib, Higher valency ion substitution into the manganese oxide framework, J. Am. Chem. Soc. 126 (2004) 7774–7775.
[6] J. Chen, X. Tang, J. Liu, E. Zhan, J. Li, X. Huang, W. Shen, Synthesis and characterization of Ag-hollandite nanofibers and its catalytic application in ethanol oxidation, Chem. Mater. 19 (2007) 4292–4299.
[7] S.H. Lee, T.W. Kim, D.H. Park, J.-H. Choy, S.-J. Hwang, N. Jiang, S.-E. Park, Y.-H. Lee, Single-step synthesis, characterization, and application of nanostructured $K_xMn_{1-y}Co_yO_{2-\delta}$ with controllable chemical compositions and crystal structures, Chem. Mater. 19 (2007) 5010–5017.
[8] X. Tang, J. Li, J. Hao, Significant enhancement of catalytic activities of manganese oxide octahedral molecular sieve by marginal amount of doping vanadium, Catal. Commun. 11 (2010) 871–875.
[9] L. Sun, Q.Q. Cao, B.Q. Hu, J.H. Li, J.M. Hao, G.H. Jing, X.F. Tang, Synthesis, characterization and catalytic activities of vanadium-cryptomelane manganese oxides in low-temperature NO reduction with NH3, Appl. Catal. A: Gen. 393 (2011) 323–330.
[10] Q. Zhang, X. Cheng, C. Zheng, X. Feng, G. Qiu, W. Tan, F. Liu, Roles of manganese oxides in degradation of phenol under UV–vis irradiation: adsorption, oxidation, and photocatalysis, J. Environ. Sci. 23 (2011) 1904–1910.
[11] J. Hou, L. Liu, Y. Li, M. Mao, H. Lv, X. Zhao, Tuning the K^+ concentration in the tunnel of OMS-2 nanorods leads to a significant enhancement of the catalytic activity for benzene oxidation, Environ. Sci. Technol. 47 (2013) 13730–13736.
[12] G. Liu, S. Liao, D. Zhu, Y. Hua, W. Zhou, Innovative photocatalytic degradation of polyethylene film with boron-doped cryptomelane under UV and visible light irradiation, Chem. Eng. J. 213 (2012) 286–294.
[13] C. Almquist, M. Krekeler, L. Jiang, An investigation on the structure and catalytic activity of cryptomelane-type manganese oxide materials prepared by different synthesis routes, Chem. Eng. J. 252 (2014) 249–262.
[14] J.R. Kona, C.K. King'ondu, A.R. Howell, S.L. Suib, OMS-2 for aerobic, catalytic one-pot alcohol oxidation-wittig reactions: efficient access to α,β-unsaturated esters, ChemCatChem 6 (2014) 749–752.
[15] H.-J. Cui, J.-W. Shi, M.-L. Fu, Synthesis and catalytic activity of magnetic cryptomelane-type manganese oxide nanotubes, J. Cluster Sci. 23 (2012) 607–614.
[16] S. Yang, W. Zhu, J. Wang, Z. Chen, Catalytic wet air oxidation of phenol over CeO_2–TiO_2 catalyst in the batch reactor and the packed-bed reactor, J. Hazard. Mater. 153 (2008) 1248–1253.
[17] R. Asahi, T. Morikawa, T. Ohwaki, K. Aoki, Y. Taga, Visible-light photocatalysis in nitrogen-doped titanium oxides, Science 293 (2001) 269–271.
[18] H. Tian, J. He, L. Liu, D. Wang, Effects of textural parameters and noble metal loading on the catalytic activity of cryptomelane-type manganese oxides for formaldehyde oxidation, Ceram. Int. 39 (2013) 315–321.
[19] J. Luo, Q. Zhang, J. Garcia-Martinez, S.L. Suib, Adsorptive and acidic properties, reversible lattice oxygen evolution, and catalytic mechanism of cryptomelane-type manganese oxides as oxidation catalysts, J. Am. Chem. Soc. 130 (2008) 3198–3207.
[20] X. Chen, Y.-F. Shen, S.L. Suib, C.L. O'Young, Characterization of manganese oxide octahedral molecular sieve (M-OMS-2) materials with different metal cation dopants, Chem. Mater. 14 (2002) 940–948.
[21] C.K. King'ondu, N. Opembe, C.-H. Chen, K. Ngala, H. Huang, A. Iyer, H.F. Garcés, S.L. Suib, Manganese oxide octahedral molecular sieves (OMS-2) multiple framework substitutions: a new route to OMS-2 particle size and morphology control, Adv. Funct. Mater. 21 (2011) 312–323.
[22] J. Cai, J. Liu, W.S. Willis, S.L. Suib, Framework doping of iron in tunnel structure cryptomelane, Chem. Mater. 13 (2001) 2413–2422.
[23] X. Shen, A.M. Morey, J. Liu, Y. Ding, J. Cai, J. Durand, Q. Wang, W. Wen, W.A. Hines, J.C. Hanson, J. Bai, A.I. Frenkel, W. Reiff, M. Aindow, S.L. Suib, Characterization of the Fe-doped mixed-valent tunnel structure manganese oxide KOMS-2, J. Phys. Chem. C 115 (2011) 21610–21619.
[24] C. Calvert, R. Joesten, K. Ngala, J. Villegas, A. Morey, X. Shen, S.L. Suib, Synthesis, characterization, and rietveld refinement of tungsten-framework-doped porous manganese oxide (K-OMS-2) material, Chem. Mater. 20 (2008) 6382–6388.
[25] J. Liu, V. Makwana, J. Cai, S.L. Suib, M. Aindow, Effects of alkali metal and ammonium cation templates on nanofibrous cryptomelane-type manganese oxide octahedral molecular sieves (OMS-2), J. Phys. Chem. B 107 (2003) 9185–9194.
[26] V.P. Santos, O.S.G.P. Soares, J.J.W. Bakker, M.F.R. Pereira, J.J.M. Órfão, J. Gascon, F. Kapteijn, J.L. Figueiredo, Structural and chemical disorder of cryptomelane promoted by alkali doping: influence on catalytic properties, J. Catal. 293 (2012) 165–174.
[27] T. Gao, P. Norby, Frame Stability of tunnel-structured cryptomelane nanofibers: the role of tunnel cations, Eur. J. Inorg. Chem. 2013 (2013) 4948–4957.
[28] H.C. Genuino, Y. Meng, D.T. Horvath, C.-H. Kuo, M.S. Seraji, A.M. Morey, R.L. Joesten, S.L. Suib, Enhancement of catalytic activities of octahedral molecular sieve manganese oxide for total and preferential CO oxidation through vanadium ion framework substitution, ChemCatChem 5 (2013) 2306–2317.
[29] W. Xu, Z. Deng, G. Li, Facile preparation of nanocryptomelane and its application in the treatment of aqueous solutions containing basic fuchsin, Ind. Eng. Chem. Res. 51 (2012) 16188–16195.
[30] H. Sun, S. Chen, P. Wang, X. Quan, Catalytic oxidation of toluene over manganese oxide octahedral molecular sieves (OMS-2) synthesized by different methods, Chem. Eng. J. 178 (2011) 191–196.
[31] Q. Zhang, Z. Xiao, X. Feng, W. Tan, G. Qiu, F. Liu, α-MnO_2 nanowires transformed from precursor δ-MnO_2 by refluxing under ambient pressure: The key role of pH and growth mechanism, Mater. Chem. Phys. 125 (2011) 678–685.
[32] R. Hu, C. Yan, L. Xie, Y. Cheng, D. Wang, Selective oxidation of CO in rich hydrogen stream over Ag/OMS-2 catalyst, Int. J. Hydrogen Energy 36 (2011) 64–71.
[33] R.M. McKenzie, The synthesis of birnessite, cryptomelane, and some other oxides and hydroxides of manganese, Mineral. Mag. 38 (1971) 493–503.
[34] N. Kijima, H. Yasuda, T. Sato, Y. Yoshimura, Preparation and characterization of open tunnel oxide α-MnO2 precipitated by ozone oxidation, J. Solid State Chem. 159 (2001) 94–102.
[35] H. Yin, F. Liu, X.H. Feng, T.D. Hu, L.R. Zheng, G.H. Qiu, L.K. Koopal, W.F. Tan, Effects of Fe doping on the structures and properties of hexagonal birnessites

– comparison with Co and Ni doping, Geochim. Cosmochim. Acta 117 (2013) 1–15.
[36] H. Yin, H. Li, Y. Wang, M. Ginder-Vogel, G. Qiu, X. Feng, L. Zheng, F. Liu, Effects of Co and Ni co-doping on the structure and reactivity of hexagonal birnessite, Chem. Geol. 381 (2014) 10–20.
[37] H. Sun, G. Qiu, Y. Wang, X. Feng, H. Yin, F. Liu, Effects of Co and Ni co-doping on the physicochemical properties of cryptomelane and its enhanced performance on photocatalytic degradation of phenol, Mater. Chem. Phys. 148 (2014) 783–789.
[38] M. Zhu, B. Legg, H. Zhang, B. Gilbert, Y. Ren, J.F. Banfield, G.A. Waychunas, Early stage formation of iron oxyhydroxides during neutralization of simulated acid mine drainage solutions, Environ. Sci. Technol. 46 (2012) 8140–8147.
[39] B. Ravel, M. Newville, ATHENA, ARTEMIS, HEPHAESTUS data analysis for X-ray absorption spectroscopy using IFEFFIT, J. Synchrotron Radiat. 12 (2005) 537–541.
[40] S.D. Kelly, D. Hesterberg, B. Ravel, Analysis of soils and minerals using X-ray absorption spectroscopy, in: A.L. Ulrey, R.L. Drees (Eds.), Methods of Soil Analysis, Part 5-Mineralogical Methods, Soil Science Society of America, 2008.
[41] S.M. Webb, SIXPACK: a graphical user interface for XAS analysis using IFEFFIT, Phys. Scr. T115 (2005) 1011–1014.
[42] J.J. Rehr, S.I. Zabinsky, R.C. Albers, High-order multiple scattering calculations of X-ray-absorption fine structure, Phys. Rev. Lett. 69 (1992) 3397–3400.
[43] A.C. Cismasu, F.M. Michel, J.F. Stebbins, C. Levard, G.E. Brown Jr., Properties of impurity-bearing ferrihydrite I. Effects of Al content and precipitation rate on the structure of 2-line ferrihydrite, Geochim. Cosmochim. Acta 92 (2012) 275–291.
[44] S. Grangeon, A. Manceau, J. Guilhermet, A.C. Gaillot, M. Lanson, B. Lanson, Zn sorption modifies dynamically the layer and interlayer structure of vernadite, Geochim. Cosmochim. Acta 85 (2012) 302–313.
[45] H.W. Nesbitt, D. Banerjee, Interpretation of XPS Mn(2p) spectra of Mn oxyhydroxides and constraints on the mechanism of MnO_2 precipitation, Am. Mineral. 83 (1998) 305–315.
[46] B.J. Tan, K.J. Klabunde, P.M.A. Sherwood, X-ray photoelectron spectroscopy studies of solvated metal atom dispersed catalysts. Monometallic iron and bimetallic iron-cobalt particles on alumina, Chem. Mater. 2 (1990) 186–191.
[47] A. Manceau, M.A. Marcus, S. Grangeon, Determination of Mn valence states in mixed-valent manganates by XANES spectroscopy, Am. Mineral. 97 (2012) 816–827.
[48] D.A. McKeown, J.E. Post, Characterization of manganese oxide mineralogy in rock varnish and dendrites using X-ray absorption spectroscopy, Am. Mineral. 86 (2001) 701–713.
[49] A. Manceau, J.M. Combes, Structure of Mn and Fe oxides and oxyhydroxides: a topological approach by EXAFS, Phys. Chem. Miner. 15 (1988) 283–295.
[50] R. Shannon, Revised effective ionic radii and systematic studies of interatomic distances in halides and chalcogenides, Acta Crystallogr. Sect. A 32 (1976) 751–767.
[51] A. Manceau, V.A. Drits, E.J. Silvester, C. Bartoli, B. Lanson, Structural mechanism of Co^{2+} oxidation by the phyllomanganate buserite, Am. Mineral. 82 (1997) 1150–1175.
[52] M. Zhu, B.W. Puls, C. Frandsen, J.D. Kubicki, H. Zhang, G.A. Waychunas, In situ structural characterization of ferric iron dimers in aqueous solutions: identification of μ-Oxo species, Inorg. Chem. 52 (2013) 6788–6797.
[53] K.D. Kwon, Keith Refson, G. Sposito, On the role of Mn(IV) vacancies in the photoreductive dissolution of hexagonal birnessite, Geochim. Cosmochim. Acta 73 (2009) 4142–4150.
[54] C. Lume-Pereira, S. Baral, A. Henglein, E. Janata, Chemistry of colloidal manganese dioxide. 1. Mechanism of reduction by an organic radical (a radiation chemical study), J. Phys. Chem. 89 (1985) 5772–5778.
[55] T. Gao, M. Glerup, F. Krumeich, R. Nesper, H. Fjellvåg, P. Norby, Microstructures and spectroscopic properties of cryptomelane-type manganese dioxide nanofibers, J. Phys. Chem. C 112 (2008) 13134–13140.
[56] Z. Guo, R. Ma, G. Li, Degradation of phenol by nanomaterial TiO_2 in wastewater, Chem. Eng. J. 119 (2006) 55–59.
[57] F. Cavani, L. Maselli, S. Passeri, J.A. Lercher, Catalytic methylation of phenol on MgO – surface chemistry and mechanism, J. Catal. 269 (2010) 340–350.
[58] E. Grabowska, J. Reszczyńska, A. Zaleska, Mechanism of phenol photodegradation in the presence of pure and modified-TiO_2: a review, Water Res. 46 (2012) 5453–5471.
[59] M. Abecassis-Wolfovich, M.V. Landau, A. Brenner, M. Herskowitz, Catalytic wet oxidation of phenol with Mn–Ce-based oxide catalysts: impact of reactive adsorption on toc removal, Ind. Eng. Chem. Res. 43 (2004) 5089–5097.
[60] C. Fan, A. Lu, Y. Li, C. Wang, Pretreatment of actual high-strength phenolic wastewater by manganese oxide method, Chem. Eng. J. 160 (2010) 20–26.
[61] Y.-S. Ding, X.-F. Shen, S. Sithambaram, S. Gomez, R. Kumar, V.M.B. Crisostomo, S.L. Suib, M. Aindow, Synthesis and catalytic activity of cryptomelane-type manganese dioxide nanomaterials produced by a novel solvent-free method, Chem. Mater. 17 (2005) 5382–5389.
[62] O. Legrini, E. Oliveros, A.M. Braun, Photochemical processes for water treatment, Chem. Rev. 93 (1993) 671–698.